

1 **A synthesis of upper ocean geostrophic kinetic energy
2 spectra from a global submesoscale permitting
3 simulation**

4 **Hemant Khatri^{1*}, Stephen M. Griffies^{1,2}, Takaya Uchida³, Han Wang⁴,
5 Dimitris Menemenlis⁵**

6 ¹Atmospheric and Oceanic Sciences Program, Princeton University, Princeton, New Jersey, USA
7 ²NOAA Geophysical Fluid Dynamics Laboratory, Princeton, New Jersey, USA

8 ³Institut des Géosciences de l'Environnement, Centre National de la Recherche Scientifique, Grenoble,
9 France

10 ⁴Department of Physics, University of Toronto, Toronto, Canada

11 ⁵Jet Propulsion Laboratory, California Institute of Technology, Pasadena, California, USA

12 **Key Points:**

- 13 • Seasonality in the upper ocean turbulence is explained as a combination of QG
14 turbulence, surface-QG turbulence, and frontal dynamics.
- 15 • Both k^{-3} and k^{-2} power-laws coexist in the horizontal wavenumber spectrum of
16 geostrophic kinetic energy in late autumn months.
- 17 • A wavenumber estimate is derived to predict the transition from the enstrophy-
18 cascading to buoyancy-variance-cascading inertial range.

* Atmospheric and Oceanic Sciences Program, 300 Forrestal Road, Sayre Hall, Princeton, NJ 08540-6654,
USA

Corresponding author: Hemant Khatri, hkhatri@princeton.edu

19 **Abstract**

20 A submesoscale-permitting global ocean model is used to study the upper ocean turbulence.
 21 Submesoscale processes peak in winter and, consequently, geostrophic kinetic energy (KE)
 22 spectra tend to be relatively shallow in winter ($\sim k^{-2}$) with steeper spectra
 23 in summer ($\sim k^{-3}$). This seasonal transition from steep to shallow power-law in the KE
 24 spectra indicates a transition from quasi-geostrophic (QG) turbulence in summer to pro-
 25 nounced surface-QG-like turbulence in winter. It is shown that this transition in KE spec-
 26 tral scaling has two phases. In the first phase (late autumn), KE spectra show a pres-
 27 ence of two spectral regimes: $\sim k^{-3}$ scaling in mesoscales (100 – 300 km) and $\sim k^{-2}$
 28 scaling in submesoscales (< 50 km), indicating the coexistence of QG, surface-QG, and
 29 frontal dynamics. In the second phase (late winter), mixed-layer instabilities convert avail-
 30 able potential energy into KE, which cascades upscale leading to flattening of the KE
 31 spectra at larger scales, and k^{-2} power-law develops in mesoscales too.

32 **Plain Language Summary**

33 Mesoscale (100 – 300 km) and submesoscale (1 – 50 km) motions are important
 34 for heat and material transport in the oceans. In the upper ocean, submesoscale turbu-
 35 lence shows seasonal variability and is pronounced in winter, whereas mesoscale turbu-
 36 lence has less seasonal variations. The same distinction is reflected in horizontal wavenum-
 37 ber spectra of KE and spectral energy fluxes. In this study, geostrophic KE spectra are
 38 analyzed in a submesoscale-permitting global ocean model to study the seasonal vari-
 39 ability in the upper ocean turbulence. We interpret the results in terms of different phys-
 40 ical mechanisms and their effects on the evolution of KE spectra over an annual cycle.
 41 We find that both mesoscale and submesoscale processes contribute to their character-
 42 ization.

43 **1 Introduction**

44 In the mid-latitudes, ocean flows at length scales of order 100 km or larger are pre-
 45 dominantly geostrophic so that the flow is quasi-two-dimensional and the Rossby num-
 46 ber is small ($Ro < 1$). Consequently, mesoscale (wavelengths roughly 100 – 300 km)
 47 turbulence is generally in accord with theories of two-dimensional turbulence (Kraichnan,
 48 1967) and quasi-geostrophic (QG) turbulence (Charney, 1971). A key feature of such the-
 49 ories is the prediction of an inverse cascade of kinetic energy (KE) at scales greater than
 50 the baroclinic Rossby deformation scale (Gkioulekas & Tung, 2007b). In accord with QG
 51 turbulence, numerous studies have observed an upscale (or inverse) transfer of KE at length
 52 scales larger than about 200 km in the upper ocean (Aluie et al., 2017; Arbic et al., 2014;
 53 Schlösser & Eden, 2007; Scott & Wang, 2005; Tulloch et al., 2011) and a forward (or down-
 54 scale) transfer of enstrophy at smaller scales accompanied by $\sim k^{-3}$ power-law in KE
 55 spectra (Khatri et al., 2018).

56 In the upper ocean, submesoscale (wavelengths roughly 1 – 50 km, $Ro \sim 1$) tur-
 57 bulence plays an equally important role in the inter-scale energy transfer with correspond-
 58 ing effects on KE spectra (Capet, McWilliams, et al., 2008a, 2008b). Submesoscale pro-
 59 cesses such as frontogenesis (Haine & Marshall, 1998; McWilliams et al., 2015) and mixed-
 60 layer baroclinic instabilities (Boccaletti et al., 2007; Fox-Kemper et al., 2008) show a sig-
 61 nificant seasonal variability with the strongest activity in winter (Mensa et al., 2013; Rocha,
 62 Gille, et al., 2016; Sasaki et al., 2017). This seasonal variability is reflected in subme-
 63 soscale KE spectra, which tend to follow k^{-2} power-law in winter and k^{-3} in summer
 64 (Callies et al., 2015; Uchida et al., 2017). In fact, spectral scaling in mesoscale KE spec-
 65 tra is also seen to vary between k^{-2} to k^{-3} depending on the region of interest (Wortham
 66 & Wunsch, 2014; Xu & Fu, 2012).

67 It has been hypothesized that wintertime submesoscale dynamics near the ocean
 68 surface agree with surface-QG turbulence. In a surface-QG regime, buoyancy variance
 69 cascades downscale, which in turn leads to $k^{-5/3}$ power-law in potential energy (PE) and
 70 KE spectra (Blumen, 1978; Held et al., 1995; Lapeyre, 2017; Pierrehumbert et al., 1994;
 71 Sukhatme & Pierrehumbert, 2002), while KE is expected to cascade upscale (Capet, Klein,
 72 et al., 2008). However, surface-QG theory does not account for secondary ageostrophic
 73 motions, which are important in frontogenesis processes (Hoskins & Bretherton, 1972).
 74 Surface-QG dynamics support the formation of strong buoyancy gradients, and, if the
 75 horizontal advection due to the ageostrophic flow component is considered, asymmetries
 76 develop in the divergence field and in the structure of vertical velocity associated with
 77 filaments (Badin, 2013; Ragone & Badin, 2016). These asymmetries tend to form dis-
 78 continuities in velocity and buoyancy fields resulting in the formation of sharp frontal
 79 structures. Consequently, k^{-2} spectral scaling (characteristic of a Heaviside step func-
 80 tion) develops in geostrophic KE spectra (Boyd, 1992; Callies & Ferrari, 2013; Klein et
 81 al., 2008). Nevertheless, a downscale cascade of buoyancy variance is expected (Sukhatme
 82 & Smith, 2009). Hence, as we argue in this paper, the k^{-2} scaling in upper ocean sub-
 83 mesoscale KE spectra in winter is consistent with surface-QG-like turbulence. To avoid
 84 ambiguity, we refer to surface-QG turbulence in the presence of fronts and secondary ageostrophic
 85 motions as “frontal-surface-QG turbulence” in the rest of the paper.

86 On the contrary, an upscale KE transfer due to mixed-layer instabilities can flat-
 87 ten the KE spectrum, as QG theory predicts $k^{-5/3}$ scaling in the inverse KE cascade in-
 88 erial range (Charney, 1971), and result in $\sim k^{-2}$ scaling at submesoscales in the win-
 89 ter KE spectrum (Boccaletti et al., 2007; Klein et al., 2008). In fact, there is evidence
 90 of inverse KE cascade even in the submesoscale range (Capet, McWilliams, et al., 2008b;
 91 Dong et al., 2020; Sasaki et al., 2017; Schubert et al., 2020). Note that these interpre-
 92 tations of KE spectra hold for the geostrophically balanced part of the flow field, which
 93 is the focus of our study. If the ageostrophic component is considered in the KE spec-
 94 trum, the presence of gravity waves can result in a k^{-2} spectral scaling at submesoscales
 95 (Garrett & Munk, 1975; Rocha, Gille, et al., 2016; Torres et al., 2018). A more detailed
 96 discussion of various ocean turbulence theories can be found in Callies and Ferrari (2013).

97 Submesoscale processes are crucial for ocean heat uptake and material transport
 98 (Su et al., 2018; Uchida et al., 2019), and understanding the physics of seasonality in sub-
 99 mesoscales is a key to understanding the impacts of submesoscale processes on mesoscale
 100 dynamics and the large-scale circulation. Moreover, studying upper-ocean submesoscale
 101 dynamics has applications for the upcoming Surface Water and Ocean Topography satel-
 102 lite mission, which aims to provide measurements at submesoscales (Fu & Ubelmann,
 103 2014).

104 In this study, we characterize how geostrophic turbulence in mesoscales and sub-
 105 mesoscales in the ocean surface mixed-layer transitions seasonally from being QG-like
 106 in summer to frontal-surface-QG-like in winter. We frame our interpretations accord-
 107 ing to the following theoretical predictions: for QG turbulence, KE spectra follow k^{-3}
 108 scaling associated with the forward enstrophy cascade (Callies & Ferrari, 2013; Char-
 109 ney, 1971); for frontal-surface-QG turbulence, KE spectra follow k^{-2} scaling associated
 110 with the forward cascade of buoyancy variance (Blumen, 1978; Boyd, 1992). We use the
 111 output from a submesoscale-permitting global ocean model to study the behavior of up-
 112 per ocean geostrophic turbulence in different parts of the world. Specifically, we analyze
 113 the temporal evolution of geostrophic KE spectral slopes, i.e., transition from k^{-3} in sum-
 114 mer to k^{-2} to winter. For the first time, we show a simultaneous presence of two power-
 115 laws (k^{-3} and k^{-2}) in geostrophic KE spectra, indicating the coexistence of QG and frontal-
 116 surface-QG turbulence. Further, we propose a wavenumber estimate to predict the tran-
 117 sition point from k^{-3} to k^{-2} scaling. The role of mixed-layer instabilities is also discussed.

118 The paper is organized as the following. The model details and methods are pro-
 119 vided in section 2, with results then presented in sections 3 and 4. We conclude the pa-
 120 per in section 5.

121 2 Methods

122 We analyze output from the 14-month (Sept 2011 to Nov 2012) LLC4320 global
 123 ocean simulation ($1/48^\circ$ horizontal grid spacing with 90 vertical levels) performed us-
 124 ing the Massachusetts Institute of Technology general circulation model (Marshall et al.,
 125 1997; Rocha, Gille, et al., 2016). LLC4320 output is appropriate for studying submesoscale
 126 processes since the model resolves dynamical processes with length scales as small as 10 km
 127 (Rocha, Gille, et al., 2016). LLC4320 output has been employed in several works to study
 128 geostrophic dynamics at mesoscales and submesoscales as well as to understand inter-
 129 actions between balanced motions and inertia-gravity waves (Chereskin et al., 2019; Dong
 130 et al., 2020; Qiu et al., 2018; Rocha, Chereskin, et al., 2016; Rocha, Gille, et al., 2016;
 131 Torres et al., 2018). We use LLC4320 output to study the interplay between mesoscale
 132 and submesoscale turbulence in the upper ocean. For this purpose, we analyzed ten $10^\circ \times$
 133 10° mid-latitude regions away from continental boundaries. Also, the ocean depth is at
 134 least 1 km in these regions so that we expect topographic effects to be minimal. Most
 135 energetic ocean mesoscale eddies are generally 100–300 km, so that the $10^\circ \times 10^\circ$ do-
 136 mains are large enough to contain mesoscale turbulence. Five of the regions are in rel-
 137 atively high KE locations, e.g., near the Gulf Stream, Kuroshio Current, and in the South-
 138 ern Ocean. The other five regions are in relatively low KE locations (see Figure 1). Re-
 139 cently, Sasaki et al. (2017) observed significant differences in the nature of submesoscale
 140 turbulence between high and low KE regions in the North Pacific. With our choice of
 141 domains, we investigate the nature of mesoscale and submesoscale turbulence in a range
 142 of dynamically different locations in the mid-latitudes.

143 In LLC4320 output, the essential fields are available as hourly snapshots for the
 144 entire duration of the simulation. We compute horizontal wavenumber spectra of KE ($\mathbf{u}^2/2$,
 145 where \mathbf{u} is the horizontal velocity) and PE ($b^2/2N^2$, b is buoyancy and N is buoyancy
 146 frequency) using velocity and density fields at different depths. In particular, we perform
 147 a Helmholtz decomposition of the two-dimensional velocity spectra to compute the KE
 148 spectra of the rotational and divergent components (Callies & Ferrari, 2013; Bühler et
 149 al., 2014; Uchida et al., 2017). For the spectral computations, we use snapshots rather
 150 than daily-averaged fields. Although time-averaging is useful in removing high-frequency
 151 inertia-gravity waves from the flow field, it can also suppress balanced submesoscale mo-
 152 tions, which have typical timescales of $\mathcal{O}(1)$ day (McWilliams, 2016; Uchida et al., 2019).
 153 Thus, time-averaging may suppress seasonal variability at submesoscales. Also, spectra
 154 obtained from time-averaged fields tend to be relatively steeper than spectra computed
 155 using snapshots (see Figure 3 in Sinha et al., 2019). This artifact would compromise our
 156 ability to compare spectral slopes against theoretical predictions. We used velocity and
 157 density snapshots at 12-hour intervals and at seven vertical levels down to 650 m depth,
 158 with seasonally and monthly-averaged spectra examined. Prior to computations, hor-
 159 izontal spatial linear trends were removed from each data snapshot (Uchida et al., 2017)
 160 and the Planck-taper windowing function was used to make the fields doubly-periodic
 161 (McKeehan et al., 2010). We provide further details on the spectra calculations in sup-
 162 porting information.

163 3 Seasonality in submesoscale KE spectra

164 Figures 2a-2h show the mean rotational KE spectra [$K^\psi(k)$] and the ratio of di-
 165 vergent to rotational KE spectra [$K^\phi(k)/K^\psi(k)$] for summer and winter seasons in dif-
 166 ferent geographic regions. In agreement with previous studies (Rocha, Gille, et al., 2016;
 167 Uchida et al., 2017), the spectral slopes in rotational KE spectra in the upper-ocean show

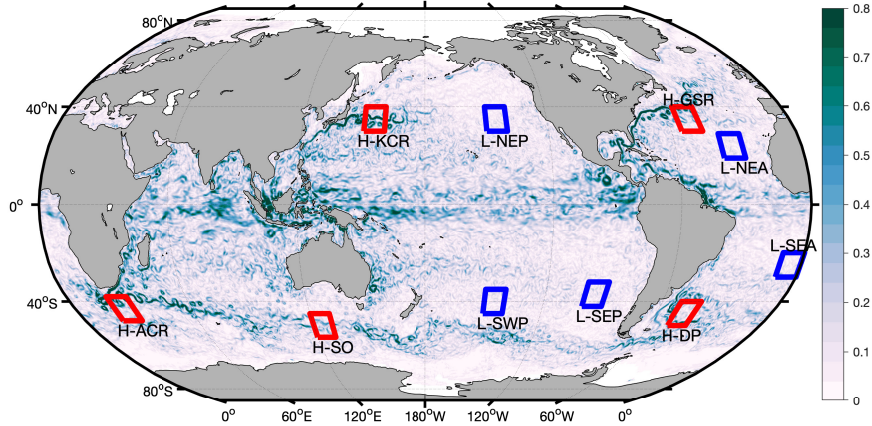


Figure 1. Ten $10^\circ \times 10^\circ$ regions chosen for the spectral analysis. High KE regions (acronyms start with ‘H’) are shown with red rectangles while blue rectangles represent relatively low KE regions (acronyms start with ‘L’). Ocean surface geostrophic speed (m/s) on 15th March 2012 from satellite altimetry dataset is shown in color.

seasonal variability (Figures 2a-2d). The rotational KE spectra (at 21 m depth) in winter are shallower than in summer, whereby they follow a power-law scaling close to k^{-2} at 10-100 km length scales in winter and k^{-3} in summer. This seasonal variability is due to the seasonal strengthening of submesoscale activity in the upper ocean, with submesoscale KE and vorticity magnitudes peaking in the winter season (Dong et al., 2020; Rocha, Gille, et al., 2016; Sasaki et al., 2017).

As seen in Figures 2e-2h, the ageostrophic (divergent) contributions in the upper-ocean can be as large as the geostrophic (rotational) ones within the submesoscale range, especially in the summer season and in low KE regions. Nevertheless, in the winter season, upper ocean submesoscale flows are predominantly rotational, which indicates that they are in near geostrophic balance. Note that rotational and geostrophic spectra are not necessarily equivalent due to the presence of weak vertical velocities associated with the balanced flow (Wang & Bühler, 2020). However, we expect the correction to be insignificant in the upper ocean because $K^\phi(k)/K^\psi(k)$ is mostly smaller than 1, especially in winter (Figures 2e-2h). Thus, this technical distinction is not important for the analysis presented in this paper. In the following, we consider just the rotational KE spectra as we are interested in geostrophic turbulence.

3.1 Wintertime KE spectra and associated spectral scaling

In the summer, k^{-3} power-law in KE spectra at mesoscales and submesoscales agrees with QG turbulence (Charney, 1971). On the other hand, k^{-2} scaling in winter KE spectra can be understood, in part, in terms of surface-QG dynamics (Blumen, 1978; Klein et al., 2008; Lapeyre, 2009), in which surface buoyancy drives the dynamics. Importantly,

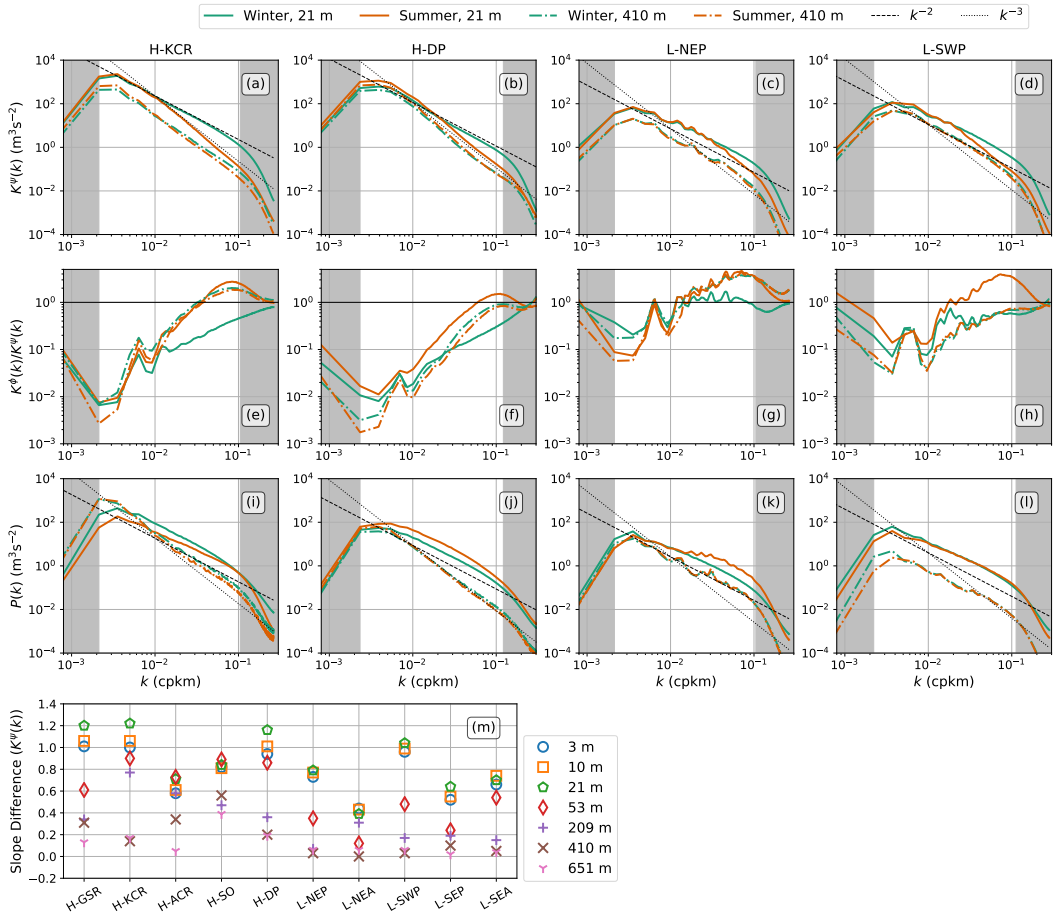


Figure 2. Seasonally-averaged (JJA and DJF) (a-d) rotational KE spectra, (e-f) the ratio of divergent to rotational KE spectra, and (i-l): PE spectra. Each is shown versus isotropic horizontal wavenumber $k = \sqrt{k_x^2 + k_y^2}$ (cycles/km) in selected high and low KE regions at depths of 21 m and 410 m. Gray patches indicate the wavenumbers over which boundary effects (low wavenumbers) and viscous dissipation (high wavenumbers) alter the spectra significantly and so are outside our scope. (m) The differences between the summer and winter spectral slopes (linear fits were computed in the wavenumber range [0.02, 0.06] cpkm) for rotational KE spectra.

the k^{-2} power-law in the winter KE spectra is steeper than the surface-QG prediction of $k^{-5/3}$ in the buoyancy-variance cascading inertial range (Blumen, 1978). With the inclusion of sharp fronts and filaments in surface-QG dynamics (referred to as frontal-surface-QG dynamics here), KE spectra are expected to fall as k^{-2} (Boyd, 1992; Callies & Ferrari, 2013). Thus, the enhanced wintertime submesoscale turbulence and associated k^{-2} scaling in KE spectra agree with frontal-surface-QG dynamics.

Alternatively, the relatively shallow k^{-2} scaling in the mesoscale KE spectra in winter can also arise from an upscale KE transfer due to mixed-layer instabilities, in which perturbations grow by extracting PE from lateral buoyancy gradients (Boccaletti et al., 2007; Callies et al., 2016; Capet, McWilliams, et al., 2008b). In this case, the spectral slope in the KE spectrum at scales larger than the mixed-layer deformation scale is expected to be controlled by two processes: an upscale KE transfer due to mixed-layer instabilities (Boccaletti et al., 2007) and a forward enstrophy transfer due to interior baroclinic instability (Charney, 1971). The QG theory predicts a $k^{-5/3}$ power-law for the KE

204 spectrum in the inverse KE cascade and k^{-3} power-law in the forward enstrophy cas-
 205 cade inertial ranges, respectively (Charney, 1971). Thus, the simulated KE spectral slope
 206 of roughly k^{-2} could also be the result of an overlap of these two cascades in wintertime
 207 submesoscale KE spectra.

208 In winter, we expect KE production at two distinct length scales: baroclinic Rossby
 209 deformation scale and mixed-layer deformation scale. Lilly (1989) first proposed to study
 210 geostrophic turbulence in the presence of two forcing length scales, and this approach
 211 may be useful in understanding the nature of upper ocean turbulence. Further, at scales
 212 smaller than the mixed-layer deformation scale, a downscale buoyancy variance flux can
 213 affect the spectral slope significantly as in surface-QG dynamics. In a recent work, Dong
 214 et al. (2020) argued that both the inverse KE transfer and forward buoyancy variance
 215 transfer contribute to shaping the k^{-2} scaling in submesoscale KE spectra. However, there
 216 is no clarity on the relative importance of the two processes nor on the evolution of KE
 217 spectra from summer to winter. We provide insight into these issues in section 4.

218 3.2 Spectra in the ocean interior

219 Thus far we have focused on the upper ocean spectra at 21 m depth. For compar-
 220 ison, in Figures 2a-2d we also show the mean rotational KE spectra at 410 m depth. Lit-
 221 ttle seasonal variability is seen at this interior depth. In Figure 2m, we show the differ-
 222 ences between the summer and winter spectral slopes (computed in the submesoscale wavenum-
 223 ber range [0.02, 0.06] cpkm) in rotational KE spectra as a function of depth. The sea-
 224 sonal variability is pronounced in the upper 50 m, where the slope differences are close
 225 to 1, and can be associated with the seasonality in the mixed layer depth, which varies
 226 between 10-20 m in summer and 100-150 m in winter (de Boyer Montégut et al., 2004).
 227 For completeness, we also assess seasonally-averaged PE spectra ($P(k)$ in Figure 2i-2l,
 228 see supporting information for computational details), which do not indicate any sea-
 229 sonal variability in spectral slopes. However, spectral slope magnitudes can differ between
 230 the ocean surface and ocean interior (Callies & Ferrari, 2013; Callies et al., 2016).

231 4 Interplay among QG turbulence, frontal-surface-QG turbulence, and 232 mixed-layer instabilities

233 Here, we examine how the upper ocean KE spectra evolve from summer to win-
 234 ter. In Figure 3a, monthly-averaged rotational KE spectra for July, November, and March
 235 are shown in the Kuroshio Current region (H-KCR). As discussed in Section 3, the KE
 236 spectra follow close to k^{-3} scaling in July whereas the scaling is close to k^{-2} in March
 237 due to enhanced submesoscale activity. In the transition month of November, the KE
 238 spectrum shows both spectral scalings, with k^{-3} at length scales larger than about 40 km
 239 and k^{-2} at smaller length scales.

240 4.1 Interpreting the dual power-laws

241 The presence of dual power-laws in the November KE spectrum indicates the co-
 242 existence of QG and frontal-surface-QG turbulence. Tulloch and Smith (2006, 2009) in-
 243 corporated both interior and boundary dynamics in a QG model and showed that the
 244 surface KE spectrum follows a k^{-3} power-law at large scales, in agreement with QG the-
 245 ory, and the spectrum transitions to a $k^{-5/3}$ power-law at relatively small scales, in ac-
 246 cord with the traditional surface-QG theory. With the consideration of sharp fronts in
 247 surface-QG dynamics (Boyd, 1992; Callies & Ferrari, 2013), we expect a change in spec-
 248 tral scaling from k^{-3} at large scales to k^{-2} at relatively small scales in the upper ocean
 249 geostrophic KE spectra, and this change in power-law is clearly seen in the November
 250 KE spectrum (Figure 3a). Hence, k^{-3} scaling is associated with the downscale enstro-

phy flux, and k^{-2} spectral scaling is associated with the downscale buoyancy variance flux and ocean fronts (Tulloch & Smith, 2006; Callies & Ferrari, 2013).

Frontal activity is expected to strengthen in late autumn (Kazmin & Rienecker, 1996; Roden, 1980) and the length scale corresponding to the change in spectral scaling (k^{-3} to k^{-2}) may be associated with the frontogenesis scale at which lateral buoyancy gradients are strong. The time series of available PE (APE) in Figure 3b confirms that buoyancy anomalies strengthen in late autumn due to frontogenesis at submesoscales (McWilliams et al., 2015). APE peaks in late autumn and this APE slowly decays by March-April due to mixed-layer instabilities, leading to an increase in the mean enstrophy in late winter (Figure 3c). It is expected that this conversion of APE to KE at submesoscales results in an inverse KE cascade. Consequently, relatively shallow k^{-2} spectral scaling develops in the March KE spectrum, even at length scales as large as 100 km (see discussions in Dong et al., 2020; Sasaki et al., 2017).

As discussed in section 3, the spectral slope in the geostrophic KE spectrum throughout the mesoscales and submesoscales is expected to be controlled by an inverse KE flux (due to mixed-layer instabilities), forward enstrophy flux (due to interior baroclinic instability), and forward buoyancy variance flux (due to frontogenesis). The temporal evolution of KE spectral slope, APE, and enstrophy in Figures 3a-3c confirms the roles of these spectral fluxes in different months. In late winter, instabilities occur at a range of length scales and all three spectral fluxes contribute to shaping the KE spectral slope (also see Dong et al., 2020). Hence, we do not expect an inertial range at 10-100 km scales in late winter, and a theoretical power-law scaling for the KE spectrum is not possible. The appearance of k^{-2} power-law in late winter KE spectra could be a mere coincidence. Nevertheless, the flattening of the KE spectrum in winter is expected due to the inverse KE transfer from mixed-layer instabilities and is robust across the oceanic regions we analyzed.

The presence of dual power-laws in late autumn is also seen in other oceanic regions (Figures 3d-3m), especially in high KE regions. In contrast, there is no clear signature of dual spectral regimes in low KE regions. It has been suggested that seasonal variability in low KE regions is due to seasonality in the KE production rate associated with interior baroclinic instability (Sasaki et al., 2017), which could be a reason for the absence of two spectral regimes in low KE regions.

4.2 Estimating the transition wavenumber

It is natural to ask what sets the transition wavenumber between k^{-3} and k^{-2} scaling in the rotational KE spectrum in late autumn. Here, we derive an expression for predicting the transition wavenumber. In inertial ranges corresponding to downscale enstrophy and buoyancy variance cascades, QG and surface-QG turbulence theories predict the following KE spectra,

$$E_{qg}(k) = C_1 \mathcal{Z}^{2/3} k^{-3} \quad \text{and} \quad E_{sqg}(k) = C_2 \mathcal{B}^{2/3} k^{-5/3}. \quad (1)$$

Here, C_1, C_2 are constants, \mathcal{Z} is the enstrophy flux, \mathcal{B} is the buoyancy variance flux divided by the squared buoyancy frequency, $N^2 = -(g/\rho_o) d\rho(z)/dz$, where $\rho(z)$ is the mean vertical potential density profile (referenced to the sea surface) evaluated using the equation of state from Jackett and McDougall (1995). We hypothesize that both QG and surface-QG dynamics determine the geostrophic KE spectral slope (see discussions in Tulloch & Smith, 2009; Tung & Orlando, 2003) and that we can furthermore write $K^\psi(k)$ as a linear superposition of $E_{qg}(k)$ and $E_{sqg}(k)$ (Gkioulekas & Tung, 2007a)

$$K^\psi(k) = C_1 \mathcal{Z}^{2/3} k^{-3} + C_2 \mathcal{B}^{2/3} k^{-5/3}. \quad (2)$$

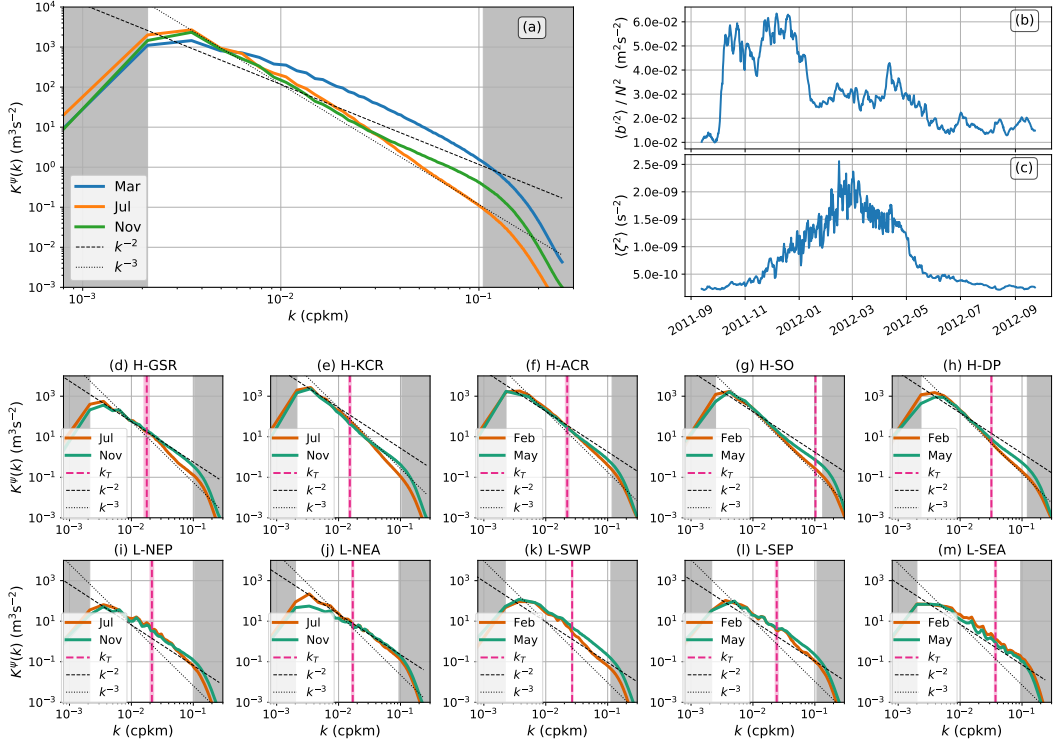


Figure 3. Panels (a-c) results at 21 m depth in the Kuroshio Current region (H-KCR) (a) monthly-averaged rotational KE spectra, (b) domain-averaged APE time series, (c) domain-averaged enstrophy time series. Panels (d-m) monthly-averaged rotational KE spectra in different regions at 21 m depth. Each is shown versus isotropic horizontal wavenumber $k = \sqrt{k_x^2 + k_y^2}$ (cycles/km) and k_T is the transition wavenumber computed using equation (4). November data was used in (d, e, i, j) and May data was used in (f-h, k-m) for computing k_T (shading represents the standard deviation in k_T).

By equating the two terms on the right hand side we obtain the following expression for the transition wavenumber

$$k_T = \left[\frac{C_1}{C_2} \right]^{3/4} \sqrt{\frac{\mathcal{Z}}{\mathcal{B}}}. \quad (3)$$

It is evident that $K^\psi(k)$ follows k^{-3} scaling at $k < k_T$ and $k^{-5/3}$ scaling at $k > k_T$. Further, we assume that the spectral flux magnitudes scale with the domain-averaged enstrophy and buoyancy variance. With this assumption, k_T (marked by vertical magenta lines in Figure 3) can be written as

$$k_T \approx \sqrt{\frac{N^2 \langle \zeta^2 \rangle}{\langle b^2 \rangle}}, \quad (4)$$

where $b = -g(\rho - \rho_o)/\rho_o$ is the buoyancy ($g = 9.8$ m/s²), ζ is the vertical component of the relative vorticity, $\langle \cdot \rangle$ is the spatial mean at a given depth, and we set $C_1 = C_2$.

As seen in Figure 3, the transition wavenumber estimates lie in the range 30-50 km (computed using the data in November and May in regions located in the Northern and Southern hemisphere, respectively) and are close to the wavenumbers at which a change in spectral scaling is found. The H-SO region is an exception and the discrepancy could

be due to the formation of deep submesoscale fronts in the Southern Ocean (Siegelman, 2020). KE spectra shown in Figure 3 were computed using the velocity field at 21 m depth but the presence of two spectral regimes is also seen at other depths (see supporting information). Note that in our k_T computations, spatial linear trends were removed from buoyancy and vorticity fields to avoid complications arising from domain-scale north-south temperature gradients. We emphasize that the k_T estimate in equation (4) suffers from the many limitations of scaling arguments. In particular, $C_1 = C_2$ need not hold and spectral flux magnitudes, which we assumed to be constant, generally vary as a function of wavenumber (Khatri et al., 2018). Moreover, we do not account for the presence of fronts.

In Figure 3, we note a time lag of about two months between APE and enstrophy peaks (a time lag is also present in other regions, see supporting information). Dong et al. (2020) observed a similar time lag between the mixed-layer depth maximum and submesoscale KE maximum. So although strong lateral buoyancy gradients are created in late autumn and result in a significant increase in APE, mixed-layer instabilities peak around late winter. This time lag is the key reason why we find two spectral regimes in Figure 3. Equation (4) inherently assumes that domain-averaged enstrophy and buoyancy variance are independent and do not affect each other, which is not expected to hold at all times. As seen in Figure 3, mixed-layer baroclinic instabilities convert APE into KE, which reduces buoyancy variance and increases enstrophy. Nevertheless, the k_T estimate works well in late autumn as mixed-layer instabilities are not as active.

Our analysis suggests that the temporal evolution of upper ocean submesoscale turbulence can be divided into two phases. In the first phase (late autumn), frontogenesis processes create strong lateral buoyancy gradients resulting in two spectral regimes (k^{-3} and k^{-2}) in the geostrophic KE spectrum. In the second phase (late winter), mixed-layer baroclinic instabilities convert APE into KE at submesoscales, and KE cascades upscale leading to a relatively shallow k^{-2} scaling in the KE spectrum at scales as large as 100 km. We provide a schematic in Figure 4 explaining the two phases. Also, k_T estimates in Figure 3 are quite close to the most unstable mixed-layer instability length scales (Figure 1 in Sasaki et al., 2017). This similarity in length scales is expected since submesoscale front length scales and mixed-layer instability scales generally overlap (Hosegood et al., 2006).

5 Discussion and Conclusions

In this study, we used output from a $1/48^\circ$ global ocean simulation to examine the behavior of upper ocean geostrophic turbulence in different parts of the World Ocean. In agreement with previous studies, we found a strong seasonality in submesoscale turbulence and the associated geostrophic kinetic energy (KE) spectra (Callies et al., 2015; Rocha, Gille, et al., 2016; Sasaki et al., 2017). Specifically, rotational KE spectra tend to follow $\sim k^{-3}$ power-law in summer in accord with QG turbulence (Charney, 1971), and $\sim k^{-2}$ power-law in winter. It is shown that mesoscale and submesoscale turbulence in the upper ocean geostrophic flows can be understood as a combination of quasi-geostrophic (QG), surface-QG, and frontal dynamics.

We described two distinct physical phases in the seasonal transition of upper ocean rotational KE spectra from k^{-3} scaling in summer to k^{-2} scaling in winter. The first phase occurs in late autumn, during which strong lateral buoyancy gradients are created due to frontogenesis at submesoscales (McWilliams et al., 2015). As a result, KE spectra develop two spectral regimes consistent with the coexistence of QG and surface-QG-like turbulence (Tulloch & Smith, 2006, 2009). Specifically, KE spectra decay as k^{-3} at length scales > 50 km associated with the forward enstrophy cascade in QG turbulence (Charney, 1971), whereas KE spectra follow k^{-2} spectral scaling at length scales < 50 km in agreement with the forward buoyancy variance cascade in surface-QG turbulence and the pres-

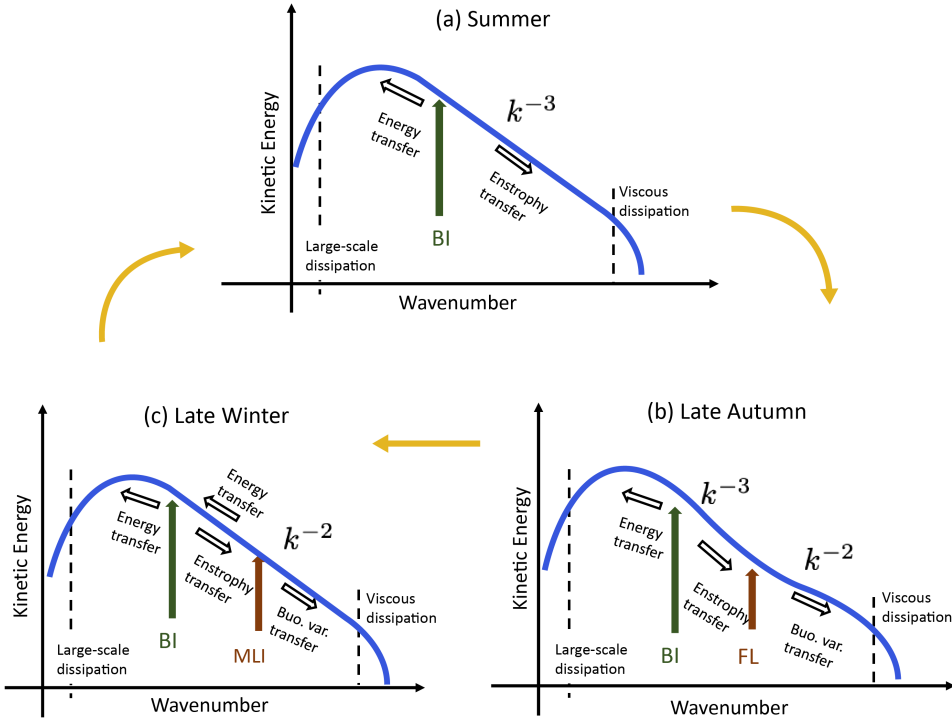


Figure 4. Schematic for the annual cycle of the geostrophic KE spectrum in the upper ocean. (a) From QG turbulence, the summer KE spectrum follows k^{-3} scaling associated with a downscale enstrophy cascade in scales smaller than baroclinic instability length scale (BI) and an inverse KE cascade is present at larger scales. (b) In late autumn, strong lateral buoyancy gradients are created due to frontogenesis (FL indicates the length scale where transition in spectral slope occurs due to the presence of fronts) and buoyancy variance cascades downscale leading to flattening of the KE spectrum to k^{-2} in submesoscales in accord with surface-QG turbulence plus frontal activity. (c) Mixed-layer baroclinic instabilities (MLI indicates the corresponding length scale) extract energy from lateral buoyancy gradients resulting in an upscale cascade of KE. Consequently, both upscale KE flux and downscale enstrophy flux affect the spectral slope, and a shallower $\sim k^{-2}$ scaling develops in the mesoscale KE spectrum. Black arrows denote the directions of the spectral fluxes of KE, enstrophy, and buoyancy variance (note that dimensions of these fluxes are different from each other).

ence of frontal structures (Blumen, 1978; Callies & Ferrari, 2013). Using the mean enstrophy and buoyancy variance magnitudes, we derived a scaling estimate for the wavenumber where the spectral scaling transitions from k^{-3} to k^{-2} . The estimated wavenumbers are able to predict the change in spectral scaling in KE spectra reasonably well. Also, available potential energy (APE) peaks during this time as strong lateral buoyancy gradients are present.

In the second phase, which peaks in late winter, mixed-layer baroclinic instabilities convert APE into KE at submesoscales, thus leading to an inverse KE cascade (see also Dong et al., 2020; Sasaki et al., 2017). Consequently, k^{-2} spectral scaling develops in KE spectra at scales of 10-100 km. We present a schematic in Figure 4 that summarizes the physical mechanisms involved with these seasonal transitions, thus depicting our finding that geostrophic turbulence in the upper ocean can be understood in terms

375 of QG, surface-QG, and frontal dynamics, with the relative importance of these processes
 376 varying seasonally.

377 Another key finding of this work is that a time lag of about 2-3 months occurs be-
 378 tween the maxima in APE due to frontogenesis and its conversion to submesoscale KE
 379 through mixed-layer baroclinic instabilities (also see Dong et al., 2020). Although fron-
 380 togenesis processes start in late autumn, mixed-layer baroclinic instabilities peak in late
 381 winter. Current submesoscale mixed-layer parameterization schemes do not account for
 382 this time lag, and APE is converted into KE instantly in the mixed-layer (Fox-Kemper
 383 et al., 2008). In practice, however, some ocean models use temporal smoothing to ob-
 384 tain more realistic circulation. For example, the GFDL-OM4 ocean climate model uses
 385 30 days as the time-scale for temporal smoothing (Adcroft et al., 2019). Currently, these
 386 time scale magnitudes are tuned to match model output to ocean measurements. How-
 387 ever, physical reasoning is missing for this temporal smoothing. We are pursuing research
 388 to determine a scaling-argument-based relation for the time scale for use in submesoscale
 389 parameterization schemes.

390 Acknowledgments

391 The idea of this study originated at the summer school “Fundamental aspects of
 392 turbulent flows in climate dynamics” in summer 2017 at École de Physique des Houches,
 393 France. Discussions with Jai Sukhatme, Jörn Callies, Raffaele Ferrari, Dhruv Balwada,
 394 Brian Arbic, Oliver Bühler, Ryan Abernathey, and Shafer Smith were helpful in this study.
 395 The authors thank Elizabeth Yankovsky and Marion Alberty for comments on the manuscript.
 396 The authors would like to thank the team maintaining the PANGEO platform (<https://pangeo.io/>), which was used for computations in this work. The authors are grateful
 397 to Catherine Raphael for help with Figure 4. LLC4320 simulation data used in this work
 398 is available on the ECCO data portal (<https://data.nas.nasa.gov/ecco/data.php>).
 399 Hemant Khatri is sponsored through award NA18OAR4320123 from the National Oceanic
 400 and Atmospheric Administration, U.S. Department of Commerce. The statements, find-
 401 ings, conclusions, and recommendations are those of the author(s) and do not necessar-
 402 ily reflect the views of the National Oceanic and Atmospheric Administration, or the U.S.
 403 Department of Commerce. Dimitris Menemenlis carried out research at the Jet Propul-
 404 sion Laboratory, California Institute of Technology, under contract with NASA, with sup-
 405 port from the Physical Oceanography and Modeling, Analysis, and Prediction Programs.
 406 High-End computing was provided by NASA Advanced Supercomputing at Ames Re-
 407 search Center.

409 References

- 410 Adcroft, A., Anderson, W., Balaji, V., Blanton, C., Bushuk, M., Dufour, C. O., ...
 411 others (2019). The gfdl global ocean and sea ice model om4. 0: Model descrip-
 412 tion and simulation features. *Journal of Advances in Modeling Earth Systems*,
 413 11(10), 3167–3211. doi: 10.1029/2019MS001726
- 414 Aluie, H., Hecht, M., & Vallis, G. K. (2017). Mapping the energy cascade in the
 415 north atlantic ocean: The coarse-graining approach. *Journal of Physical*
 416 *Oceanography*. doi: 10.1175/JPO-D-17-0100.1
- 417 Arbic, B. K., Müller, M., Richman, J. G., Shriver, J. F., Morten, A. J., Scott, R. B.,
 418 ... Penduff, T. (2014). Geostrophic turbulence in the frequency-wavenumber
 419 domain: Eddy-driven low-frequency variability. *Journal of Physical Oceanogra-*
 420 *phy*, 44(8), 2050–2069. doi: 10.1175/JPO-D-13-054.1
- 421 Badin, G. (2013). Surface semi-geostrophic dynamics in the ocean. *Geophysical*
 422 *& Astrophysical Fluid Dynamics*, 107(5), 526–540. doi: 10.1080/03091929.2012
 423 .740479
- 424 Blumen, W. (1978). Uniform potential vorticity flow: Part i. theory of wave inter-

- actions and two-dimensional turbulence. *Journal of the Atmospheric Sciences*, 35(5), 774–783. doi: 10.1175/1520-0469(1978)035<0774:UPVFPI>2.0.CO;2
- Boccaletti, G., Ferrari, R., & Fox-Kemper, B. (2007). Mixed layer instabilities and restratification. *Journal of Physical Oceanography*, 37(9), 2228–2250. doi: 10.1175/JPO3101.1
- Boyd, J. P. (1992). The energy spectrum of fronts: Time evolution of shocks in burgers' equation. *Journal of the Atmospheric Sciences*, 49(2), 128–139. doi: 10.1175/1520-0469(1992)049<0128:TESOFT>2.0.CO;2
- Bühler, O., Callies, J., & Ferrari, R. (2014). Wave-vortex decomposition of one-dimensional ship-track data. *Journal of Fluid Mechanics*, 756, 1007–1026. doi: 10.1017/jfm.2014.488
- Callies, J., & Ferrari, R. (2013). Interpreting energy and tracer spectra of upper-ocean turbulence in the submesoscale range (1–200 km). *Journal of Physical Oceanography*, 43(11), 2456–2474. doi: 10.1175/JPO-D-13-063.1
- Callies, J., Ferrari, R., Klymak, J. M., & Gula, J. (2015). Seasonality in submesoscale turbulence. *Nature Communications*, 6. doi: 10.1038/ncomms7862
- Callies, J., Flierl, G., Ferrari, R., & Fox-Kemper, B. (2016). The role of mixed-layer instabilities in submesoscale turbulence. *Journal of Fluid Mechanics*, 788, 5–41. doi: 10.1017/jfm.2015.700
- Capet, X., Klein, P., Hua, B. L., Lapeyre, G., & Mcwilliams, J. C. (2008). Surface kinetic energy transfer in surface quasi-geostrophic flows. *Journal of Fluid Mechanics*, 604, 165–174. doi: 10.1017/S0022112008001110
- Capet, X., McWilliams, J. C., Molemaker, M. J., & Shchepetkin, A. (2008a). Mesoscale to submesoscale transition in the California current system. part i: Flow structure, eddy flux, and observational tests. *Journal of Physical Oceanography*, 38(1), 29–43. doi: 10.1175/2007JPO3671.1
- Capet, X., McWilliams, J. C., Molemaker, M. J., & Shchepetkin, A. (2008b). Mesoscale to submesoscale transition in the California current system. part iii: Energy balance and flux. *Journal of Physical Oceanography*, 38(10), 2256–2269. doi: 10.1175/2008JPO3810.1
- Charney, J. (1971). Geostrophic turbulence. *Journal of the Atmospheric Sciences*, 28, 1087–1095. doi: 10.1175/1520-0469(1971)028<1087:GT>2.0.CO;2
- Chereskin, T. K., Rocha, C. B., Gille, S. T., Menemenlis, D., & Passaro, M. (2019). Characterizing the transition from balanced to unbalanced motions in the southern California current. *Journal of Geophysical Research: Oceans*, 124(3), 2088–2109. doi: 10.1029/2018JC014583
- de Boyer Montégut, C., Madec, G., Fischer, A. S., Lazar, A., & Iudicone, D. (2004). Mixed layer depth over the global ocean: An examination of profile data and a profile-based climatology. *Journal of Geophysical Research: Oceans*, 109(C12). doi: 10.1029/2004JC002378
- Dong, J., Fox-Kemper, B., Zhang, H., & Dong, C. (2020). The seasonality of submesoscale energy production, content, and cascade. *Geophysical Research Letters*, 47(6), e2020GL087388. doi: 10.1029/2020GL087388
- Fox-Kemper, B., Ferrari, R., & Hallberg, R. (2008). Parameterization of mixed layer eddies. part i: Theory and diagnosis. *Journal of Physical Oceanography*, 38(6), 1145–1165. doi: 10.1175/2007JPO3792.1
- Fu, L.-L., & Ubelmann, C. (2014). On the transition from profile altimeter to swath altimeter for observing global ocean surface topography. *Journal of Atmospheric and Oceanic Technology*, 31(2), 560–568. doi: 10.1175/JTECH-D-13-00109.1
- Garrett, C., & Munk, W. (1975). Space-time scales of internal waves: A progress report. *Journal of Geophysical Research*, 80(3), 291–297. doi: 10.1029/JC080i003p00291
- Gkioulekas, E., & Tung, K. K. (2007a). Is the subdominant part of the energy spectrum due to downscale energy cascade hidden in quasi-geostrophic tur-

- 480 turbulence? *Discrete & Continuous Dynamical Systems-B*, 7(2), 293. doi:
 481 10.3934/dcdsb.2007.7.293
- 482 Gkioulekas, E., & Tung, K. K. (2007b). A new proof on net upscale energy cascade
 483 in two-dimensional and quasi-geostrophic turbulence. *Journal of Fluid Mechanics*,
 484 576, 173. doi: 10.1017/S0022112006003934
- 485 Haine, T. W., & Marshall, J. (1998). Gravitational, symmetric, and baroclinic insta-
 486 bility of the ocean mixed layer. *Journal of physical oceanography*, 28(4), 634–
 487 658. doi: 10.1175/1520-0485(1998)028<0634:GSABIO>2.0.CO;2
- 488 Held, I. M., Pierrehumbert, R. T., Garner, S. T., & Swanson, K. L. (1995). Surface
 489 quasi-geostrophic dynamics. *Journal of Fluid Mechanics*, 282, 1–20. doi: 10
 490 .1017/S0022112095000012
- 491 Hosegood, P., Gregg, M. C., & Alford, M. H. (2006). Sub-mesoscale lateral den-
 492 sity structure in the oceanic surface mixed layer. *Geophysical Research Letters*,
 493 33(22). doi: 10.1029/2006GL026797
- 494 Hoskins, B. J., & Bretherton, F. P. (1972). Atmospheric frontogenesis models:
 495 Mathematical formulation and solution. *Journal of the Atmospheric Sciences*,
 496 29(1), 11–37. doi: 10.1175/1520-0469(1972)029<0011:AFMMFA>2.0.CO;2
- 497 Jackett, D. R., & McDougall, T. J. (1995). Minimal adjustment of hydrographic pro-
 498 files to achieve static stability. *Journal of Atmospheric and Oceanic Technol-
 499 ogy*, 12(2), 381–389. doi: 10.1175/1520-0426(1995)012<0381:MAOHPT>2.0.CO;
 500 2
- 501 Kazmin, A. S., & Rienecker, M. M. (1996). Variability and frontogenesis in the
 502 large-scale oceanic frontal zones. *Journal of Geophysical Research: Oceans*,
 503 101(C1), 907–921. doi: 10.1029/95JC02992
- 504 Khatri, H., Sukhatme, J., Kumar, A., & Verma, M. K. (2018). Surface ocean enstro-
 505 phy, kinetic energy fluxes, and spectra from satellite altimetry. *Journal of Geo-
 506 physical Research: Oceans*, 123(5), 3875–3892. doi: 10.1029/2017JC013516
- 507 Klein, P., Hua, B. L., Lapeyre, G., Capet, X., Le Gentil, S., & Sasaki, H. (2008).
 508 Upper ocean turbulence from high-resolution 3d simulations. *Journal of Physi-
 509 cal Oceanography*, 38(8), 1748–1763. doi: 10.1175/2007JPO3773.1
- 510 Kraichnan, R. H. (1967). Inertial ranges in two-dimensional turbulence. *Physics of
 511 Fluids*, 10(7), 1417–1423. doi: 10.1063/1.1762301
- 512 Lapeyre, G. (2009). What vertical mode does the altimeter reflect? on the decompo-
 513 sition in baroclinic modes and on a surface-trapped mode. *Journal of Physical
 514 Oceanography*, 39(11), 2857–2874. doi: 10.1175/2009JPO3968.1
- 515 Lapeyre, G. (2017). Surface quasi-geostrophy. *Fluids*, 2(1), 7. doi: 10.3390/
 516 fluids2010007
- 517 Lilly, D. K. (1989). Two-dimensional turbulence generated by energy sources at two
 518 scales. *Journal of the Atmospheric Sciences*, 46(13), 2026–2030. doi: 10.1175/
 519 1520-0469(1989)046<2026:TDTGBE>2.0.CO;2
- 520 Marshall, J., Adcroft, A., Hill, C., Perelman, L., & Heisey, C. (1997). A finite-
 521 volume, incompressible navier stokes model for studies of the ocean on parallel
 522 computers. *Journal of Geophysical Research: Oceans*, 102(C3), 5753–5766.
- 523 McKeechan, D., Robinson, C., & Sathyaprakash, B. S. (2010). A tapering window for
 524 time-domain templates and simulated signals in the detection of gravitational
 525 waves from coalescing compact binaries. *Classical and Quantum Gravity*,
 526 27(8), 084020. doi: 10.1088/0264-9381/27/8/084020
- 527 McWilliams, J. C. (2016). Submesoscale currents in the ocean. *Proceedings of the
 528 Royal Society A: Mathematical, Physical and Engineering Sciences*, 472(2189),
 529 20160117. doi: 10.1098/rspa.2016.0117
- 530 McWilliams, J. C., Gula, J., Molemaker, M. J., Renault, L., & Shchepetkin, A. F.
 531 (2015). Filament frontogenesis by boundary layer turbulence. *Journal of
 532 Physical Oceanography*, 45(8), 1988–2005. doi: 10.1175/JPO-D-14-0211.1
- 533 Mensa, J. A., Garraffo, Z., Griffa, A., Özgökmen, T. M., Haza, A., & Veneziani, M.
 534 (2013). Seasonality of the submesoscale dynamics in the gulf stream region.

- 535 *Ocean Dynamics*, 63(8), 923–941. doi: 10.1007/s10236-013-0633-1
- 536 Pierrehumbert, R., Held, I., & Swanson, K. (1994). Spectra of local and nonlocal
537 two-dimensional turbulence. *Chaos, Solitons & Fractals*, 4(6), 1111–1116. doi:
538 10.1016/0960-0779(94)90140-6
- 539 Qiu, B., Chen, S., Klein, P., Wang, J., Torres, H., Fu, L.-L., & Menemenlis, D.
540 (2018). Seasonality in transition scale from balanced to unbalanced motions
541 in the world ocean. *Journal of Physical Oceanography*, 48(3), 591–605. doi:
542 10.1175/JPO-D-17-0169.1
- 543 Ragone, F., & Badin, G. (2016). A study of surface semi-geostrophic turbulence:
544 freely decaying dynamics. *Journal of Fluid Mechanics*, 792, 740–774. doi: 10
545 .1017/jfm.2016.116
- 546 Rocha, C. B., Chereskin, T. K., Gille, S. T., & Menemenlis, D. (2016). Mesoscale
547 to submesoscale wavenumber spectra in drake passage. *Journal of Physical
548 Oceanography*, 46(2), 601–620. doi: 10.1175/JPO-D-15-0087.1
- 549 Rocha, C. B., Gille, S. T., Chereskin, T. K., & Menemenlis, D. (2016). Seasonality
550 of submesoscale dynamics in the kuroshio extension. *Geophysical Research Letters*,
551 43(21), 11–304. doi: 10.1002/2016GL071349
- 552 Roden, G. I. (1980). On the variability of surface temperature fronts in the west-
553 ern pacific, as detected by satellite. *Journal of Geophysical Research: Oceans*,
554 85(C5), 2704–2710. doi: 10.1029/JC085iC05p02704
- 555 Sasaki, H., Klein, P., Sasai, Y., & Qiu, B. (2017). Regionality and seasonality of sub-
556 mesoscale and mesoscale turbulence in the north pacific ocean. *Ocean Dynam-
557 ics*, 67(9), 1195–1216. doi: 10.1007/s10236-017-1083-y
- 558 Schrösser, F., & Eden, C. (2007). Diagnosing the energy cascade in a model of the
559 north atlantic. *Geophysical Research Letters*, 34(2). (L02604) doi: 10.1029/
560 2006GL027813
- 561 Schubert, R., Gula, J., Greatbatch, R. J., Baschek, B., & Biastoch, A. (2020). The
562 submesoscale kinetic energy cascade: Mesoscale absorption of submesoscale
563 mixed layer eddies and frontal downscale fluxes. *Journal of Physical Oceanog-
564 raphy*, 50(9), 2573–2589. doi: 10.1175/JPO-D-19-0311.1
- 565 Scott, R. B., & Wang, F. (2005). Direct evidence of an oceanic inverse kinetic en-
566 ergy cascade from satellite altimetry. *Journal of Physical Oceanography*, 35(9),
567 1650–1666. doi: 10.1175/JPO2771.1
- 568 Siegelman, L. (2020). Energetic submesoscale dynamics in the ocean interior. *Jour-
569 nal of Physical Oceanography*, 50(3), 727–749. doi: 10.1175/JPO-D-19-0253.1
- 570 Sinha, A., Balwada, D., Tarshish, N., & Abernathey, R. (2019). Modula-
571 tion of lateral transport by submesoscale flows and inertia-gravity waves.
572 *Journal of Advances in Modeling Earth Systems*, 11(4), 1039–1065. doi:
573 10.1029/2018MS001508
- 574 Su, Z., Wang, J., Klein, P., Thompson, A. F., & Menemenlis, D. (2018). Ocean sub-
575 mesoscales as a key component of the global heat budget. *Nature communica-
576 tions*, 9(1), 1–8. doi: 10.1038/s41467-018-02983-w
- 577 Sukhatme, J., & Pierrehumbert, R. (2002). Surface quasigeostrophic turbulence:
578 The study of an active scalar. *Chaos*, 12(2), 439–450. doi: 10.1063/1.1480758
- 579 Sukhatme, J., & Smith, L. M. (2009). Local and nonlocal dispersive turbulence.
580 *Physics of Fluids*, 21(5), 056603. doi: 10.1063/1.3141499
- 581 Torres, H. S., Klein, P., Menemenlis, D., Qiu, B., Su, Z., Wang, J., ... Fu, L.-
582 L. (2018). Partitioning ocean motions into balanced motions and inter-
583 nal gravity waves: A modeling study in anticipation of future space mis-
584 sions. *Journal of Geophysical Research: Oceans*, 123(11), 8084–8105. doi:
585 10.1029/2018JC014438
- 586 Tulloch, R., Marshall, J., Hill, C., & Smith, K. S. (2011). Scales, growth rates,
587 and spectral fluxes of baroclinic instability in the ocean. *Journal of Physical
588 Oceanography*, 41(6), 1057–1076. doi: 10.1175/2011JPO4404.1
- 589 Tulloch, R., & Smith, K. (2006). A theory for the atmospheric energy spec-

- 590 trum: Depth-limited temperature anomalies at the tropopause. *Proceedings of the National Academy of Sciences*, 103(40), 14690–14694.
591 doi: 10.1073/pnas.0605494103
- 592 Tulloch, R., & Smith, K. S. (2009). Quasigeostrophic turbulence with explicit surface dynamics: Application to the atmospheric energy spectrum. *Journal of the Atmospheric Sciences*, 66(2), 450–467. doi: 10.1175/2008JAS2653.1
- 593 Tung, K. K., & Orlando, W. W. (2003). The k- 3 and k- $5/3$ energy spectrum of
594 atmospheric turbulence: Quasigeostrophic two-level model simulation. *Journal of the atmospheric sciences*, 60(6), 824–835. doi: 10.1175/1520-0469(2003)
595 060<0824:TKAKES>2.0.CO;2
- 600 Uchida, T., Abernathey, R., & Smith, S. (2017). Seasonality of eddy kinetic energy
601 in an eddy permitting global climate model. *Ocean Modeling*, 118, 41–58. doi:
602 10.1016/j.ocemod.2017.08.006
- 603 Uchida, T., Balwada, D., Abernathey, R., McKinley, G., Smith, S., & Lévy, M.
604 (2019). The contribution of submesoscale over mesoscale eddy iron transport
605 in the open southern ocean. *Journal of Advances in Modeling Earth Systems*,
606 11(12), 3934–3958. doi: 10.1029/2019MS001805
- 607 Wang, H., & Bühler, O. (2020). Ageostrophic corrections for power spectra and
608 wave-vortex decomposition. *Journal of Fluid Mechanics*, 882. doi: 10.1017/
609 jfm.2019.815
- 610 Wortham, C., & Wunsch, C. (2014). A multidimensional spectral description of
611 ocean variability. *Journal of Physical Oceanography*, 44(3), 944–966. doi: 10
612 .1175/JPO-D-13-0113.1
- 613 Xu, Y., & Fu, L.-L. (2012). The effects of altimeter instrument noise on the estimation
614 of the wavenumber spectrum of sea surface height. *Journal of Physical Oceanography*, 42(12), 2229–2233. doi: 10.1175/JPO-D-12-0106.1
- 615